

# Surface and Subsurface Remote Sensing of Concrete Structures Using Synthetic Aperture Radar Imaging

Tzuyang Yu, A.M.ASCE<sup>1</sup>; Jones Owusu Twumasi, S.M.ASCE<sup>2</sup>; Viet Le, S.M.ASCE<sup>3</sup>; Qixiang Tang, S.M.ASCE<sup>4</sup>; and Nicolas D'Amico, S.M.ASCE<sup>5</sup>

**Abstract:** Surface and subsurface inspection of concrete structures provides useful information for the maintenance of these structures. Remote sensing techniques such as radar and microwave sensors enable engineers to assess structural condition with ease and efficiency. This paper reports the performance of a 10.5 GHz portable imaging radar system for the quantitative, surface, and subsurface sensing of concrete structures in field configuration. Ranging, size determination, crack imaging, and subsurface interface determination are conducted using stripmap synthetic aperture radar (SAR) images. Three concrete structures are selected for field measurements. Ranging accuracy, size determination procedure, and effect of background noise are studied. Issues with background subtraction are discussed. Image-based, quantitative condition assessment criteria for ranging and size determination are proposed. DOI: 10.1061/(ASCE)ST.1943-541X.0001730. © 2017 American Society of Civil Engineers.

**Author keywords:** Subsurface sensing; Synthetic aperture radar (SAR); Concrete structures; Ranging; Size determination; Crack imaging; Interface determination; Structural health monitoring.

## Introduction

Remotely inspecting concrete structures for the early detection of subsurface defects such as steel rebar corrosion is an attractive technological capability for the effective maintenance of critical civil infrastructures. Compared with surface defects (e.g., concrete cracking), subsurface defects are better candidates for early stage damage detection and structural health monitoring. Existing non-destructive testing/evaluation (NDT/E) methods are constrained by their own characteristics, preventing them from becoming practical, subsurface remote-sensing techniques. For example, ultrasonic testing (UT) can detect subsurface defects in steel structures but perfect coupling between UT transducers and the structure is usually required. Subsurface imaging applications of UT on concrete structures have been reported (Krause et al. 2001; Schickert et al. 2003; Hoegh and Khazanovich 2015). Other acoustic techniques such as impact-echo also have been applied to the imaging of concrete structures (Sansalone and Street 1997). Ground-penetrating radar (GPR) is capable of conducting subsurface profiling of road pavements and underground pipelines in either ground-coupled or air-coupled mode, but the separation distance between the GPR antenna and the target usually is less than 0.5 m (20 in.) (Bungey 2004;

Daniels 2007; Jol 2009). Other noncontact radar and microwave techniques that can perform remote sensing are for structural testing or displacement monitoring, which cannot perform subsurface inspection or sensing (Shinozuka et al. 2000; Pieraccini et al. 2004; Bennett and Rutz 2012). A recent review on the NDT/E methods for concrete bridges reported that only contact GPR techniques can perform subsurface sensing of concrete structures (Rehman et al. 2016). In other words, contact or near-contact radar/microwave methods (e.g., GPR) are capable of conducting subsurface sensing, whereas noncontact or remote radar/microwave methods can conduct surface sensing. Only a very few studies exist on the use of synthetic aperture radar (SAR) imaging for the subsurface sensing of concrete structures. Rhim and Buyukozturk (2000) reported their concrete imaging work for the detection of concrete delamination and subsurface steel rebars using three microwave bands. They demonstrated the feasibility of SAR for the subsurface delamination and rebar detection of concrete using laboratory specimens. No quantitative condition assessment criterion was reported in their work. Yu and Buyukozturk (2008) studied the use of SAR on concrete for subsurface sensing by studying the effects of inspection angle and signal bandwidth using laboratory fiber-reinforced polymer (FRP)-wrapped concrete specimens. Yu et al. (2016) combined SAR and laser acoustic sensing for the detection of subsurface delamination in laboratory FRP-wrapped concrete specimens and studied the pros and cons of hybrid NDT. Yu (2016) proposed an SAR image transformation approach (K-R-I transform) for solving the difficulties of SAR image comparison. In addition, synthetic aperture imaging also has been applied to elastic waves in the impact-echo inspection of concrete (Ganguli et al. 2012). Until now, no SAR imaging work on real concrete structures for subsurface sensing has been reported in literature.

This paper presents a SAR imaging work on real concrete structures (a composite wall, a retaining wall, and a bridge abutment) with quantitative remote-sensing criteria. This work aims at bridging the technical gap between contact or near-contact radar/microwave methods and noncontact or remote radar/microwave methods for concrete structures. This paper also reports field applications of a portable imaging radar system for the surface and subsurface remote

<sup>1</sup>Associate Professor, Dept. of Civil and Environmental Engineering, Univ. of Massachusetts Lowell, Lowell, MA 01854 (corresponding author). E-mail: tzuyang\_yu@uml.edu

<sup>2</sup>Ph.D. Student, Dept. of Civil and Environmental Engineering, Univ. of Massachusetts Lowell, Lowell, MA 01854.

<sup>3</sup>Master Student, Dept. of Civil and Environmental Engineering, Univ. of Massachusetts Lowell, Lowell, MA 01854.

<sup>4</sup>Ph.D. Student, Dept. of Civil and Environmental Engineering, Univ. of Massachusetts Lowell, Lowell, MA 01854.

<sup>5</sup>Master Student, Dept. of Civil and Environmental Engineering, Univ. of Massachusetts Lowell, Lowell, MA 01854.

Note. This manuscript was submitted on August 20, 2015; approved on October 20, 2016; published online on August 4, 2017. Discussion period open until January 4, 2018; separate discussions must be submitted for individual papers. This paper is part of the *Journal of Structural Engineering*, © ASCE, ISSN 0733-9445.

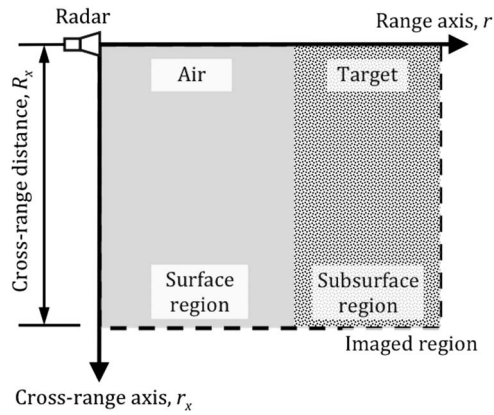


Fig. 1. Stripmap SAR imaging mode

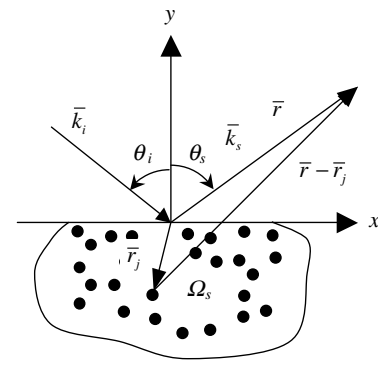


Fig. 2. Scattering of  $N$  point scatterers

sensing of concrete structures. A stripmap SAR imaging algorithm is used in the development of the portable radar system. Image-based condition assessment criteria are proposed for calculating target dimensions and determining materials property. Three reinforced concrete (RC) building and retaining walls are selected as example structures for field test.

This paper first details the imaging principle of SAR, followed by the hardware description of a portable imaging radar system. Selected example structures also are described. Imaging results are provided and discussed. Finally, research findings are summarized.

## Imaging Principle

In SAR imaging, three modes are commonly used; spotlight, stripmap, and inverse. Spotlight and inverse modes are used to acquire the SAR images with the highest resolution, whereas stripmap mode is used to scan large areas with ease. Subsurface sensing of SAR imaging usually adopts range-cross range representation (or  $r - r_x$ ). The range axis is the forward-looking direction of the radar, and the cross-range axis is the direction perpendicular to the range axis. In the stripmap SAR imaging mode, the radar scans a strip region during its operation, as shown in Fig. 1. Surface and subsurface information are imaged along the range direction when radar remote sensing is performed. This paper conducts subsurface sensing by using range-cross range SAR images.

Range-cross range SAR images are generated by backprojection algorithms (Kak and Slaney 2001). Consider a stripmap SAR imaging mode shown in Fig. 1. At each radar location, an incident wave with unit amplitude is defined by (Kong 2000)

$$\psi_{\text{inc}}(\bar{\mathbf{r}}) = \frac{1}{r} e^{i\bar{\mathbf{k}}_i \cdot \bar{\mathbf{r}}} \quad (1)$$

where  $\bar{\mathbf{k}}_i = k_{ix}\hat{\mathbf{x}} - k_{iy}\hat{\mathbf{y}}$  is the incident wave vector;  $\bar{\mathbf{r}}$  = relative position vector from the radar to any observation point;  $|\bar{\mathbf{r}}| = r$  = length of the relative position vector;  $i = \sqrt{-1}$  = imaginary number; and  $\hat{\mathbf{x}}$  and  $\hat{\mathbf{y}}$  = unit vectors in a Cartesian coordinate system. Fig. 2 illustrates the configuration of incident and scattered waves.

The scattered field from scatterer  $j$  at  $\bar{\mathbf{r}}_j$  and observed at  $\bar{\mathbf{r}}$  is

$$\psi_{\text{scat}}(\bar{\mathbf{r}}, \bar{\mathbf{r}}_j) = \frac{s_j(\bar{\mathbf{r}}, \hat{\mathbf{k}}_i)}{|\bar{\mathbf{r}} - \bar{\mathbf{r}}_j|} \cdot e^{ik|\bar{\mathbf{r}} - \bar{\mathbf{r}}_j|} \cdot \psi_{\text{inc}}(\bar{\mathbf{r}}) \quad (2)$$

where  $s_j = s_j(\bar{\mathbf{r}}, \hat{\mathbf{k}}_i)$  = scattered amplitude at scatterer  $j$  due to an incident wave at  $\hat{\mathbf{k}}_i$ , observed at  $\bar{\mathbf{r}}$ . By neglecting the interaction among scatterers (second-order effect), the total scattered field from

$N$  scatterers observed at  $\bar{\mathbf{r}}$  is the summation of the scattered fields from all scatterers. Eq. (3) represents a sliced projection of the two-dimensional (2D) Fourier transform (FT) of the domain  $\Omega_s$

$$\psi_{\text{scat}}(\bar{\mathbf{r}}) = \sum_{j=1}^N \frac{s_j(\hat{\mathbf{k}}_s, \hat{\mathbf{k}}_i)}{|\bar{\mathbf{r}} - \bar{\mathbf{r}}_j|} \cdot e^{ik|\bar{\mathbf{r}} - \bar{\mathbf{r}}_j|} \cdot \psi_{\text{inc}}(\bar{\mathbf{r}}) \quad (3)$$

where  $\bar{\mathbf{k}}_s = k_{sx}\hat{\mathbf{x}} + k_{sy}\hat{\mathbf{y}}$  = scattered wave vector; and  $\bar{\mathbf{k}}_s = -\bar{\mathbf{k}}_i$  when the radar operates in monostatic mode (single radar antenna). Without losing generality, consider the case of a single scatterer in this formulation. Knowing that  $k = \omega/c$  and  $\theta = \theta_i = \tan^{-1}(k_{iy}/k_{ix})$ , Eq. (2) can be written as

$$\psi_{\text{scat}}(\omega, \theta) = \psi_{\text{scat}}(k, \bar{\mathbf{r}}_s) = \frac{S_\theta}{r^2} \cdot \exp \left[ i \frac{r}{c} \omega (1 + \cos^2\theta - \sin^2\theta) \right] \quad (4)$$

In backprojection algorithms, one-dimensional (1D) inverse FT (IFT, line projection) is first performed to generate subimages. The final image is obtained by summing all subimages. The center in backprojection images is coincided with the center of the scatterer by performing a modulation operation in the frequency domain or a convolution operation in the time domain. The shifting-back step in the backprojection algorithm in the frequency domain is performed by applying a ramp filter in which frequency  $\omega_n$  is shifted back by a carrier frequency  $\omega_c$  (Desai and Jenkins 1992). The scattering response in subimages can be described by Eq. (5) or Eq. (6)

$$\begin{aligned} P(v, \theta) &= \int_{\omega_{\min}}^{\omega_{\max}} d\omega \cdot \psi_{\text{scat}}(\omega - \omega_c, \theta) |\omega - \omega_c| \exp(-i\omega v) \quad (5) \\ &= \frac{S_\theta}{r^2} \int_{\omega_{\min}}^{\omega_{\max}} d\omega \cdot |\omega - \omega_c| \\ &\quad \cdot \exp \times \left[ i \frac{r}{c} (\omega - \omega_c) (1 + \cos^2\theta - \sin^2\theta) - i\omega v \right] \quad (6) \end{aligned}$$

where  $v$  = spatial variable of the 1D IFT projection. Translating the local 1D IFT coordinate  $[v, P(v, \theta_s)]$  to the global polar coordinate  $(r, \theta)$  suggests that

$$v = r \cos(\phi - \theta_s) \quad (7)$$

Transforming from  $P(v, \theta)$  to  $P[r \cos(\phi - \theta), \theta]$  usually is associated with upsampling in order to improve image quality. In other words,  $P[r \cos(\phi - \theta), \theta]$  is the interpolated version of  $P(v, \theta)$ . The final backprojection (range-cross range) image is obtained by integrating the subimages along the entire synthetic aperture (cross-range axis in stripmap SAR mode).

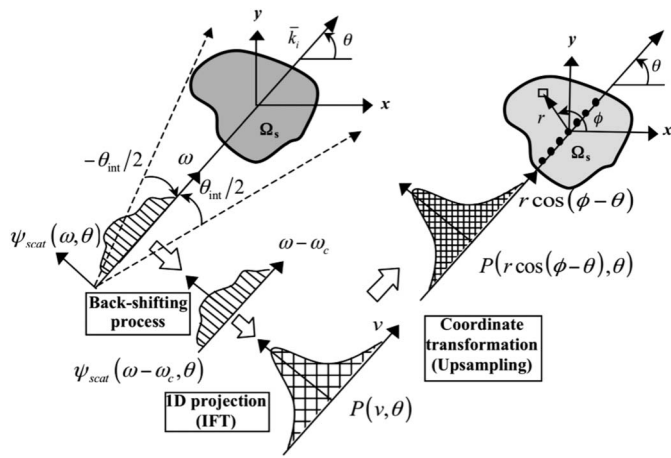


**Fig. 3.** Conceptual description of backprojection algorithms (reprinted from Yu 2011, © ASCE)

$$I(r, \phi) = \int_{-\theta_{int}/2}^{\theta_{int}/2} d\theta \cdot P[r \cos(\phi - \theta), \theta] \quad (8)$$

This process can be conceptually illustrated by Fig. 3. Eq. (8) also can be converted into its Cartesian form by

$$x = r \cos \phi \quad (9)$$

$$y = r \sin \phi \quad (10)$$

This way the range–cross range SAR images can be obtained as long as the orientation of the synthetic aperture is specified. The final backprojected SAR image amplitude  $I(r, r_x)$  in the range–cross range plane can be represented by

$$I(r, r_x) = \int_{-\infty}^{\infty} h\left(t - \frac{2r'}{c}\right) e^{-4i\pi(r'/\lambda)} \cdot A(r') \int_0^{R_x} S(r', r'_x) \cdot a\left(\frac{r_x - r'_x}{R_0}\right) e^{-iF(r_x - r'_x)^2} dr'_x dr' \quad (11)$$

where  $r$  = range;  $r_x$  = cross-range;  $h$  = matched filter;  $t$  = time;  $c$  = speed of light;  $i = \sqrt{-1}$ ;  $\lambda$  = wavelength;  $A$  = function accounting for antenna pattern, processing gain, and the range spreading loss;  $R_x$  = maximum cross-range;  $S$  = scattering amplitude;  $a$  = two-way amplitude azimuth antenna pattern;  $R_0$  = range location of the radar; and  $F$  = focusing function. Formulation of various SAR modes can be found in the literature (Soumekh 1999; Cheney 2001; Cumming and Wong 2005; Yu 2011). Computational issues related to image interpolation also can be found in the literature (Carrara et al. 1995; Soumekh 1999).

### Portable Imaging Radar System

A portable imaging radar system was designed and built for conducting stripmap SAR imaging of concrete structures in the field. This portable imaging radar system consisted of a biaxial positioner, a radar unit, and a laptop computer. The biaxial positioner moved in two cross-range directions at a 0.00625-m stepping increment. The radar unit included a signal modulator; a power amplifier; and a pyramidal, standard-gain horn antenna capable of accommodating radar signals in the frequency range of 8–18 GHz. The radar system had a 4-GHz bandwidth, suggesting a 0.0375-m range resolution. Both the radar motion and signal processing were programmed with *LabVIEW* code. A laptop computer was used as a control station and for data storage purpose. Fig. 4 shows the portable imaging radar system and the hardware design of the radar sensor.

### Field Applications

Three field test sites on the north campus of the University of Massachusetts Lowell were selected for surface (ranging, size determination, and crack imaging) and subsurface (interface determination) remote sensing using the portable imaging radar system (Fig. 5). A brick-decorated concrete wall of Olney Auditorium was selected as an example target for ranging and interface determination [Fig. 5(a)]. A reinforced concrete (RC) wall of Pinnanski Hall with a periodic trapezoidal protrusion feature was used for size

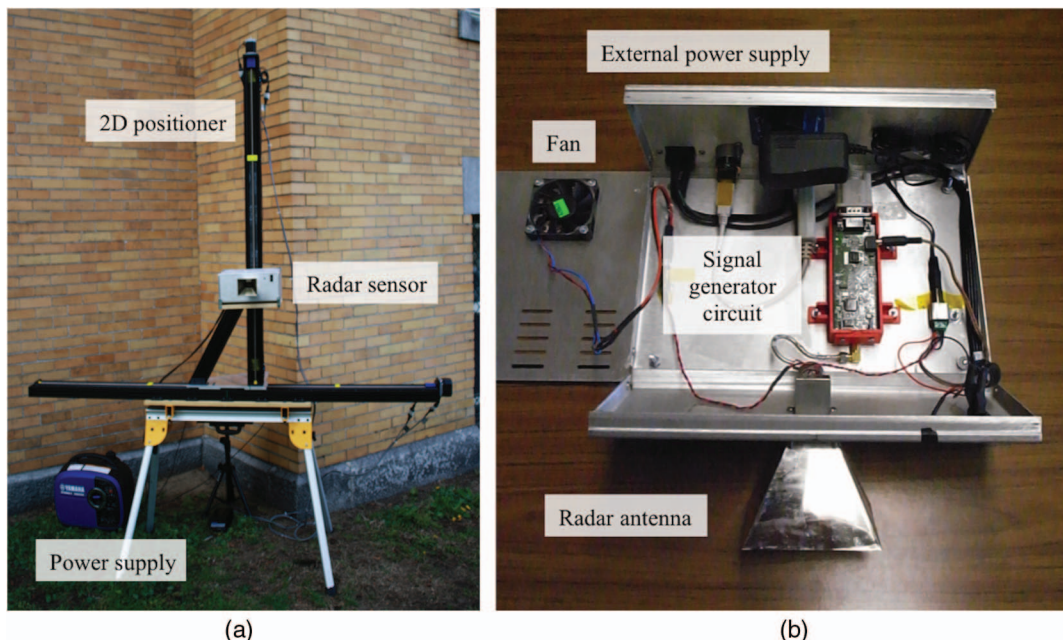


**Fig. 4.** (Color) (a) Portable radar system; (b) hardware design of the radar sensor

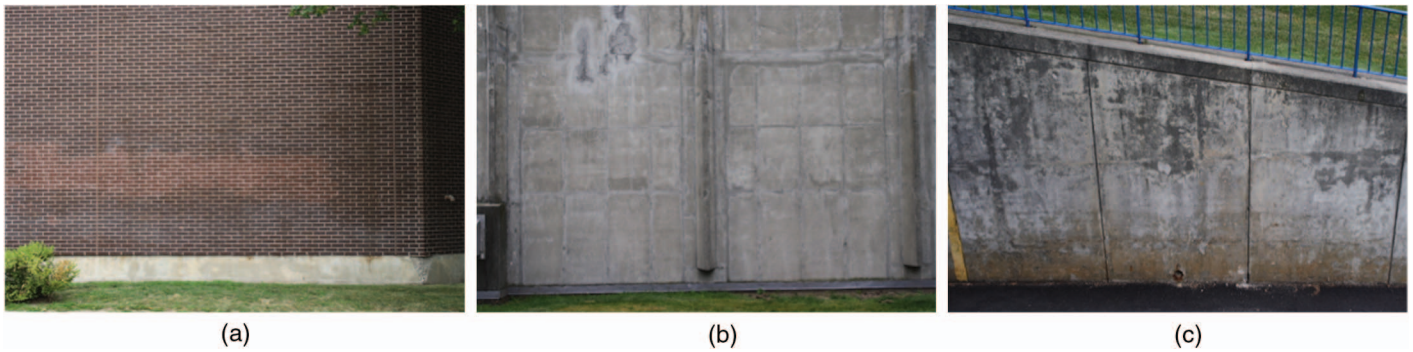


**Fig. 5.** (Color) Three field test sites for radar imaging: (a) composite wall for ranging; (b) RC wall for size determination; (c) retaining wall for crack imaging

determination [Fig. 5(b)]. An aged RC retaining wall with surface cracks in the loading dock area of Olney Auditorium was selected for crack imaging [Fig. 5(c)]. In all radar field measurements, electromagnetic background noise was expected. Three radar tests were conducted for surface and subsurface remote sensing using SAR images and are described in the following subsections.

### Building Wall for Ranging

The objective of this test was to use SAR images for ranging or range determination. As shown in Fig. 5(a), a composite (brick-concrete) wall was selected for testing the ranging capability of the radar system using SAR images. Five ranges were chosen in this test, including 1.5, 2.5, 5, 10, and 15 m. Because the radar system was positioned either parallel to or tilted at an angle with respect to the wall target along the cross-range direction, all ranges were measured at the center of the cross-range. Fig. 6 shows strip-map SAR images of the concrete wall at different ranges. Fig. 7 shows a SAR amplitude comparison at mid-cross-range along the range direction of these images.

In Fig. 6, the radar imaged both the specular return from the wall and background noise. Background noise was imaged by the SAR amplitude at 0.1-m range, representing mainly the site characteristics of the location under inspection. Background noise also included the stationary and nonstationary electromagnetic signals in the frequency range of 8–18 GHz (frequency) at the location of the wall (space) during the test (time). This test purposely avoided other possible noise sources, such as obstacles between the radar and the target. When comparing the change of specular return of the wall with the increase of range in Fig. 7, it was found, as expected, that the closer the radar, the stronger was the specular return from the wall.

In the ranging test, a SAR image-based criterion was proposed for calculating the effective range  $r_{\text{eff}}$  of a target from SAR images

$$r_{\text{eff}} = r_i(I_{\text{max}}) \quad (12)$$

where  $r_i$  = range of the maximum SAR amplitude  $I_{\text{max}}$ . Eq. (12) is the ranging criterion or the maximum amplitude criterion used in this paper. In this criterion, effective range  $r_{\text{eff}}$  is determined by the range at which the maximum SAR amplitude occurs. Fig. 8 shows the comparison of effective range and actual range with percentage error. Should the ranging criterion predict perfect range estimates, the curve in Fig. 8 should be a 45° straight line. From Fig. 8, it was found that the maximum amplitude criterion performed very well on ranging a composite wall from 1.5 to 15 m in the field test, with a maximum error of 2%.

From Fig. 7, maximum SAR amplitudes at various ranges were modeled by the following equation:

$$I_{\text{max}} = 660.21r^{-0.2647} \quad (13)$$

where  $r$  = range (m). This curve-fitting result is associated with an  $R^2$  error of 0.9953. Fig. 9 illustrates the curve-fitting result. Eq. (13) can be converted into a ranging criterion

$$r_{\text{eff}} = \left( \frac{I_{\text{max}}}{2234} \right)^{-3.7779} \quad (14)$$

Eq. (14) is the realization of the proposed ranging criterion in this application.

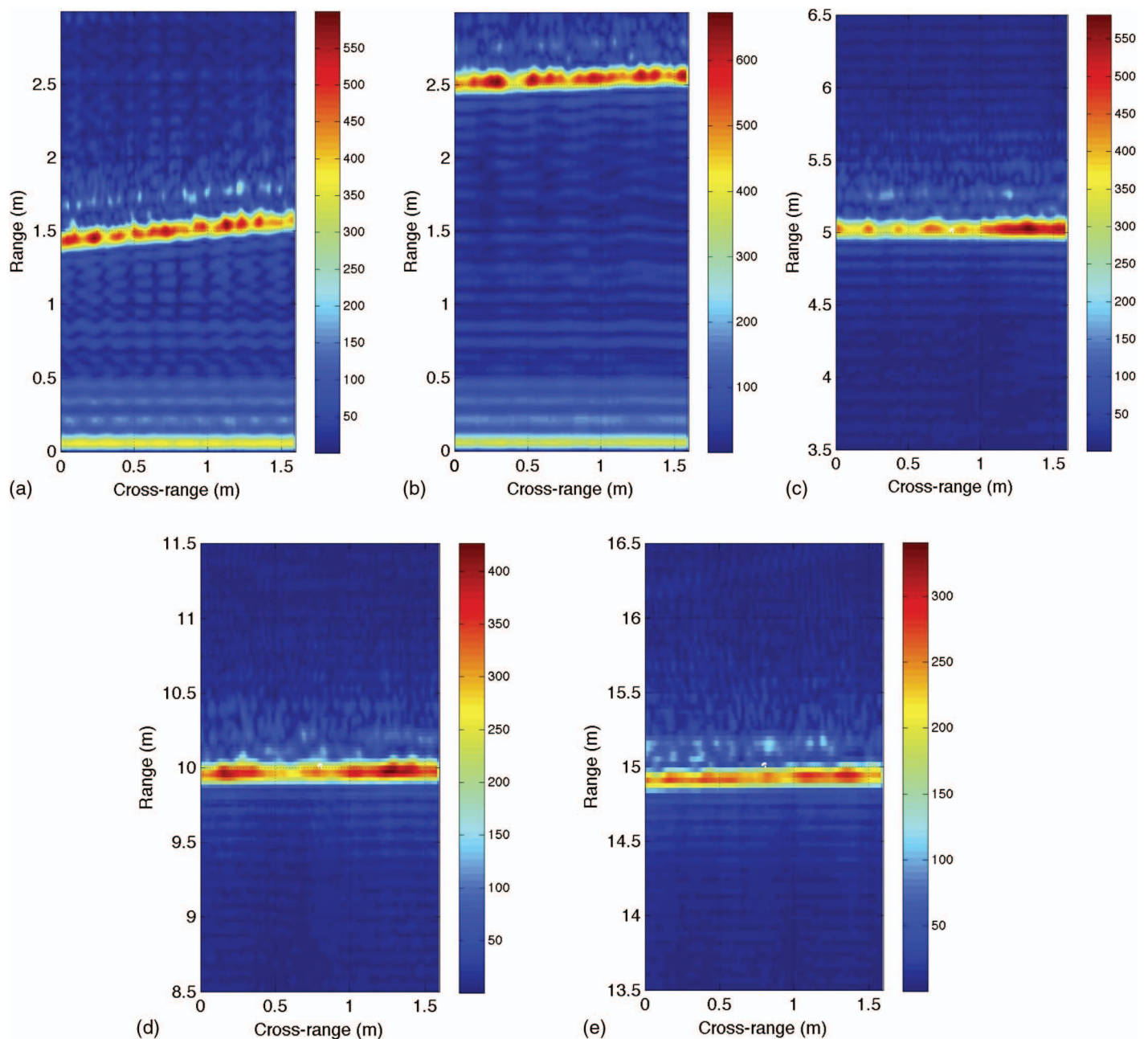
Fig. 8 also provides insights into the effect of background noise. The SAR amplitudes at short ranges indicate the electromagnetic characteristics of the background on the site (Fig. 10).

Fig. 10 shows that these background noise curves were consistent both qualitatively and quantitatively, suggesting the repeatability of these radar field measurements. The maximum SAR amplitude of background noise ( $I_{\text{bg}}$ ) was used to calculate the signal-to-noise ratio (SNR) of these results, in which  $I_{\text{max}}$  is the peak amplitude of the composite wall. Fig. 11 shows the calculated SNR values at different ranges.

In Fig. 11, SNR becomes less than unity when range exceeds 4.989 m. This means that the SAR amplitude of background noise was greater than that of the specular return of the brick wall in the field test. In other words, the effect of background noise became dominant in the SAR images generated from the ranging test of a composite wall. To reduce the effect of background noise in the range determination using SAR images, removal of short-range background noise is necessary.

Meanwhile, it was found that the specular return of the wall indicates not only the range location but also the composition of the wall. In Fig. 6(a) (range = 1.5 m), the specular return of the wall is assembled by a number of similar-sized scatterers, suggesting the periodic surface feature of the wall.

With the measured brick length being 0.22 m, there were 7.27 bricks within the cross-range of 1.6 m. In Figs. 6(a and b) (range = 1.5 and 2.5 m, respectively), 14 scatterers corresponding to two edges of a brick were identified, but a similar finding cannot be drawn from the SAR images at ranges greater than 2.5 m. This suggests that the closer the imaging radar is to a target, the higher is its ability to detect detailed features of the target.



**Fig. 6.** (Color) Stripmap SAR images of a concrete wall decorated with ceramic tiles: (a) range 1.5 m; (b) range 2.5 m; (c) range 5 m; (d) range 10 m; (e) range 15 m

### Building Wall for Size Determination

The objective of this test was to use SAR images to determine the size of a target. As shown in Fig. 5(b), a RC wall with a trapezoidal protrusion feature was chosen for size determination using SAR images. Because of the simplicity of the trapezoidal protrusion on the RC wall, it was selected for size determination (e.g., back base width  $w_b$ , front base width  $w_f$ , depth  $d$ ). Fig. 12 provides a schematic sketch of the RC wall. Actual dimensions of the protrusion were  $w_b = 0.254$  m (10 in.),  $w_f = 0.0889$  (3.5 in.), and  $d = 0.381$  m (15 in.).

Four heights of the radar were selected: 1.117, 1.617, 1.867, and 2.112 m. The range in all these SAR images was 1.5 m from the radar to the RC wall (Fig. 13). The facet of the concrete wall is illustrated by a white dashed line in Fig. 13.

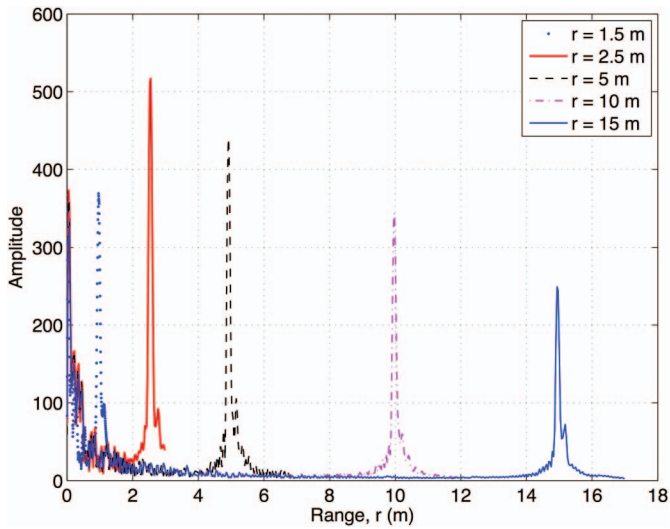
All SAR images in Fig. 13 should be identical if the concrete wall was homogeneous in the vertical direction. Differences among these images can be used to assess the heterogeneity of the concrete wall in the vertical direction. A flat area (without protrusion) on the same wall was chosen as the background signal in this test.

Analysis of SAR amplitudes in these images provides the basis for developing size-determination criteria.

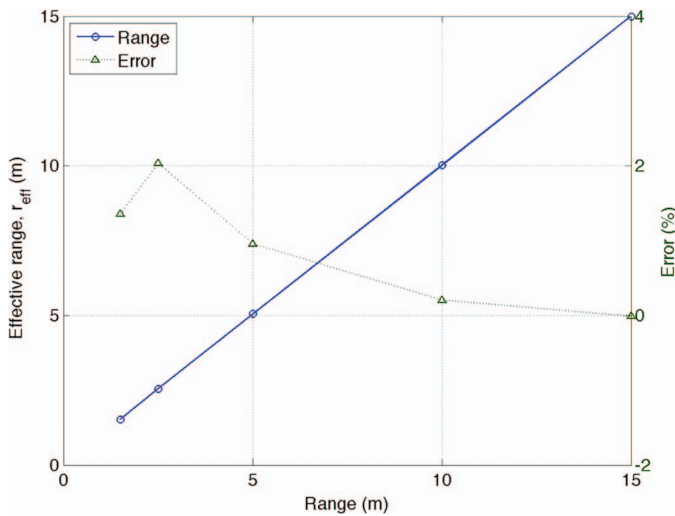
For determining the depth ( $d$ ) of the protrusion feature, a criterion based on maximum and minimum SAR amplitudes was used

$$d = r(I_{\min}) - r(I_{\max}) \quad (15)$$

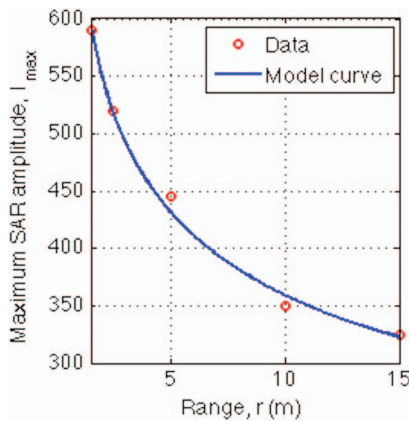
where  $r(I_{\min})$  = range at which a minimum SAR amplitude occurs; and  $r(I_{\max})$  = range at which a maximum SAR amplitude occurs.



**Fig. 7.** (Color) SAR amplitudes of a concrete wall at mid-cross-range



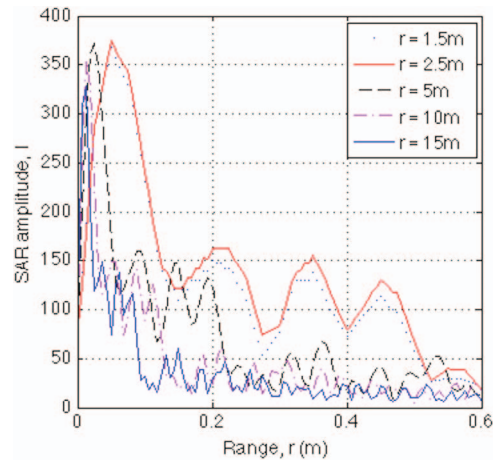
**Fig. 8.** (Color) Effective range versus actual range—concrete wall



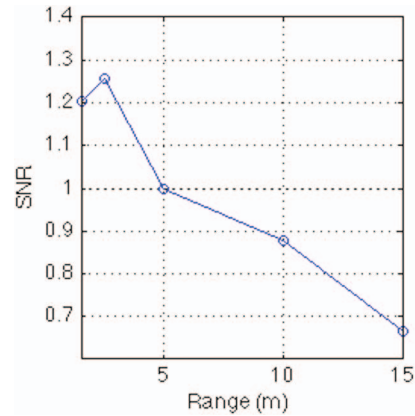
**Fig. 9.** (Color) Maximum SAR amplitude versus range

Fig. 14 shows two defined parameters in Eq. (15) for depth determination.

Fig. 15 shows the mid-cross-range amplitude curves (at 0.6 m cross-range) of four SAR images at various heights (1.117, 1.617,



**Fig. 10.** (Color) SAR amplitudes of electromagnetic background noise



**Fig. 11.** (Color) SNR values for different range measurements

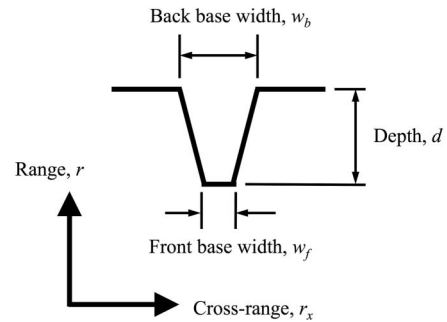


**Fig. 12.** Schematic sketch of the RC wall with protrusion

1.867, and 2.117 m). Each SAR image of Fig. 15 shows three curves representing background (without protrusion), original (with protrusion), and background-subtracted (difference) SAR amplitudes.

Table 1 summarizes the performance of the maximum and minimum amplitude criterion for depth determination by comparing the predicted depth with the actual depth (0.381 m).

For predicting the back base width ( $w_b$ ) of the protrusion, an intersecting curve criterion and a maximum amplitude criterion were used, as shown in Eqs. (16) and (17)

$$w_b = (r_x)_2 \{I|I_{\max}(r^f) \cap I_{\max}(r^b)\} - (r_x)_1 \{I|I_{\max}(r^f) \cap I_{\max}(r^b)\} \quad (16)$$

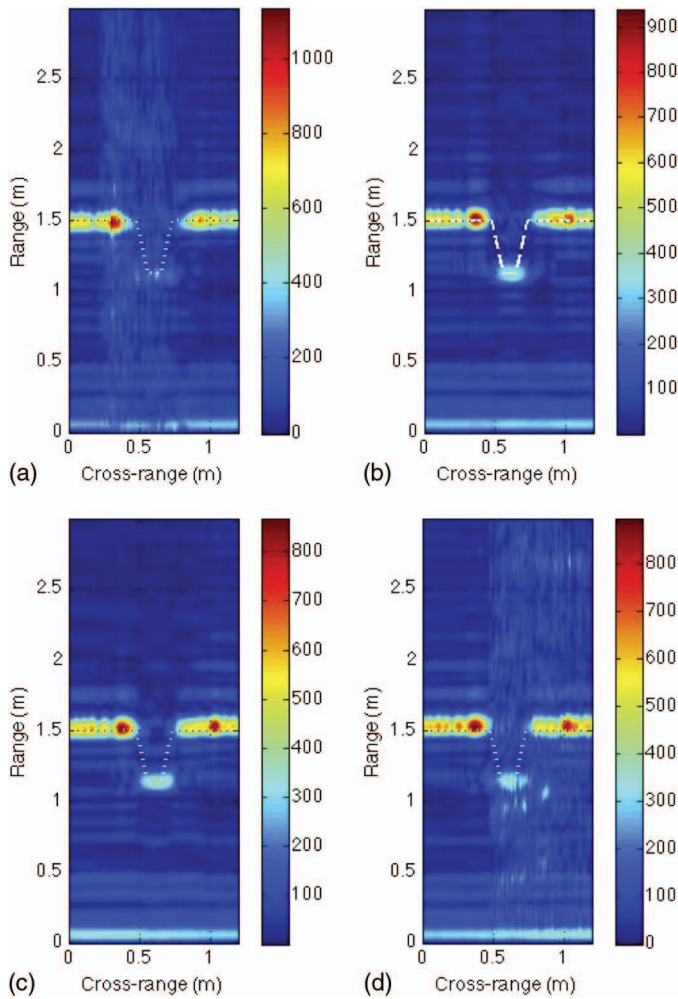


**Fig. 13.** (Color) SAR images of a RC wall at different heights: (a) 1.117 m; (b) 1.617 m; (c) 1.867 m; (d) 2.117 m

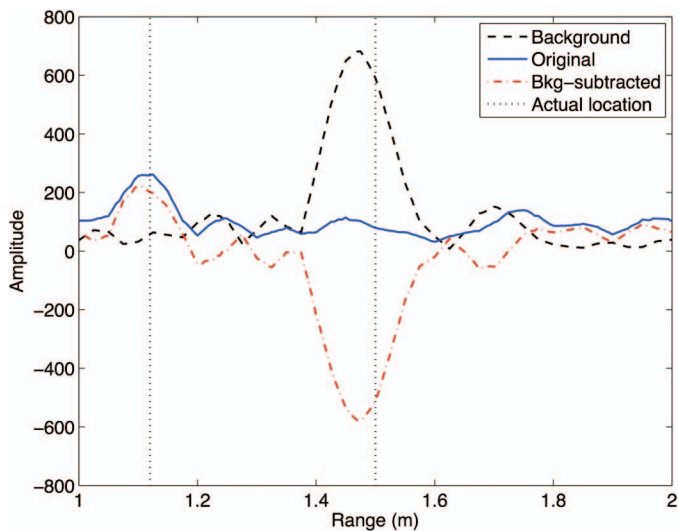


**Fig. 14.** (Color) Defined parameters used in depth determination

where  $(r_x)_2 \{I|I_{\max}(r^f) \cap I_{\max}(r^b)\}$  = cross-range value at Point 2 when the maximum SAR amplitude of front base intersects with the maximum SAR amplitude of back base; and  $(r_x)_1$  = conjugate point of  $(r_x)_2$ , both of which are defined in Fig. 15. Table 2

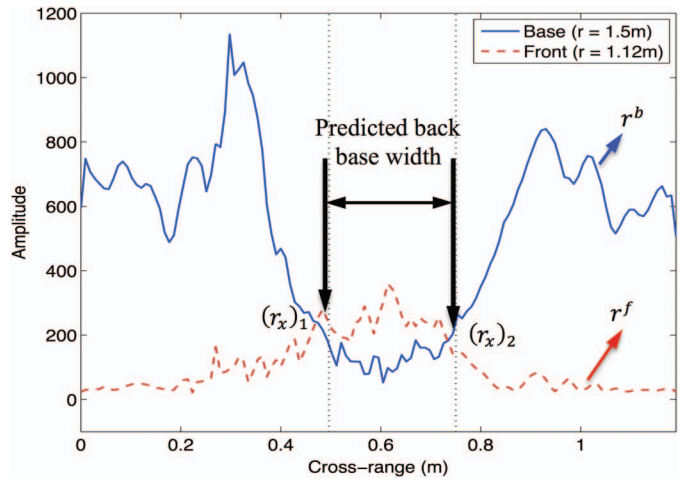


**Fig. 15.** (Color) Back base width  $w_b$  estimation—intersecting curve criterion

**Table 1.** Performance of the Depth Determination Criterion

Parameter	Height [ $H$ (m)]				Mean
	$H = 1.117$	$H = 1.617$	$H = 1.867$	$H = 2.117$	
Predicted depth (m)	0.369	0.375	0.344	0.319	0.35175
Error (%)	-3.1496	-2.3437	-9.7112	-16.2730	-7.6771

**Table 2.** Performance of the Back Base Width Determination Criterion—Intersecting Curve

Parameter	Height [ $H$ (m)]				Mean
	$H = 1.117$	$H = 1.617$	$H = 1.867$	$H = 2.117$	
Predicted width (m)	0.2652	0.2465	0.2419	0.2047	0.2396
Error (%)	4.4094	-2.9528	-4.7638	-19.4094	-5.6791

summarizes the performance of this criterion for back base determination, which has an average error of  $-5.6791\%$ .

The maximum amplitude criterion for estimating back base width  $w_b$ , uses the cross-range distance between two extreme SAR amplitudes. Fig. 16 illustrates the parameters defined in Eq. (17)

$$w_b = (r_x)_2 \{I|I_{\max}(r^f)\} - (r_x)_1 \{I|I_{\max}(r^b)\} \quad (17)$$

Table 3 summarizes the performance of Eq. (17), which has an average error of 14.3701%. Eq. (17) is the envelope criterion for predicting the front base width ( $w_f$ ) of protrusion.

A step-by-step geometric procedure is proposed for estimating the front base width  $w_f$ . Fig. 17 illustrates all defined points and lines.

1. Locate two strong scatterers (due to corner scattering; Points A and B) on the specular return of the wall in a background-subtracted SAR image. Connect the centers of these scatterers to form a line.
2. Connect Points A and B to the center of the cross-range (Point C) to form a triangle. Calculate the slopes of two legs of the triangle (AC and BC).

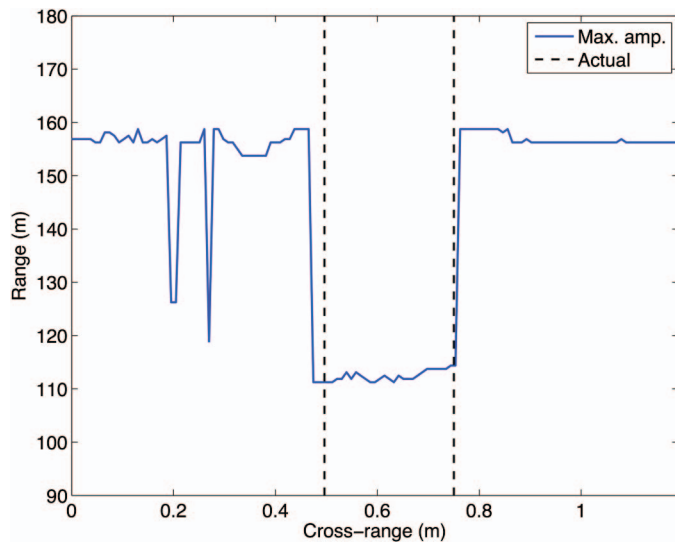


**Fig. 16.** (Color) Back base width  $w_b$  estimation—maximum amplitude criterion

**Table 3.** Performance of the Back Base Width Determination Criterion—Maximum Amplitude

Parameter	Height [ $H$ ] (m)				Mean
	$H = 1.117$	$H = 1.617$	$H = 1.867$	$H = 2.117$	
Predicted width (m)	0.3437	0.2759	0.2759	0.2665	0.2905
Error (%)	35.3150	8.6220	8.6220	4.9213	14.3701

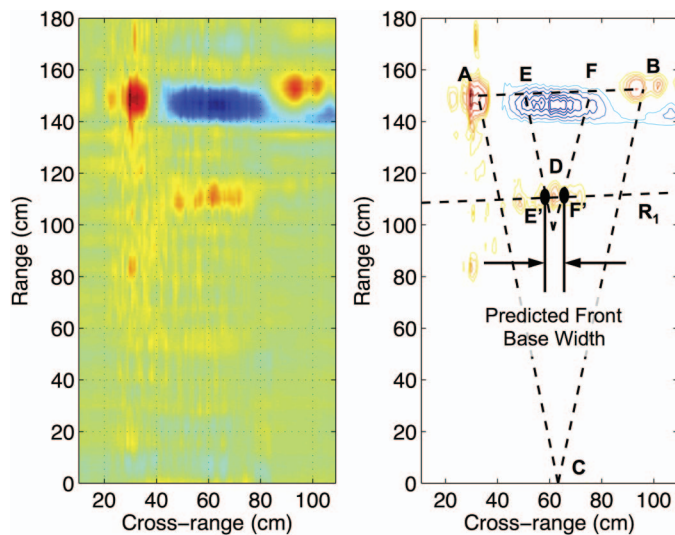


**Fig. 17.** (Color) Front base width  $w_f$  estimation—envelope criterion

3. Locate the actual back base width ( $w_b$ ) on Line AB to identify Points E and F.
4. Use the peak amplitude (Point D) on the front scatterers and the slope of Line AB to develop a reference Line  $R_1$ .
5. Use the slopes of Lines AC and BC to draw two lines intersecting  $R_1$  with Points  $E'$  and  $F'$ . Line  $F'F$  is  $L_1$ , and Line  $E'E$  is  $L_2$ .
6. The distance between Points  $E'$  and  $F'$  is the estimated front base width  $w_f$ .

**Table 4.** Performance of the Front Base Width Estimation Criterion

Parameter	Height [ $H$ ] (m)				Mean
	$H = 1.117$	$H = 1.617$	$H = 1.867$	$H = 2.117$	
Predicted width (m)	0.0651	0.0952	0.1023	0.0930	8.8900
Error (%)	-26.7537	7.0551	15.1012	4.6378	0.0000

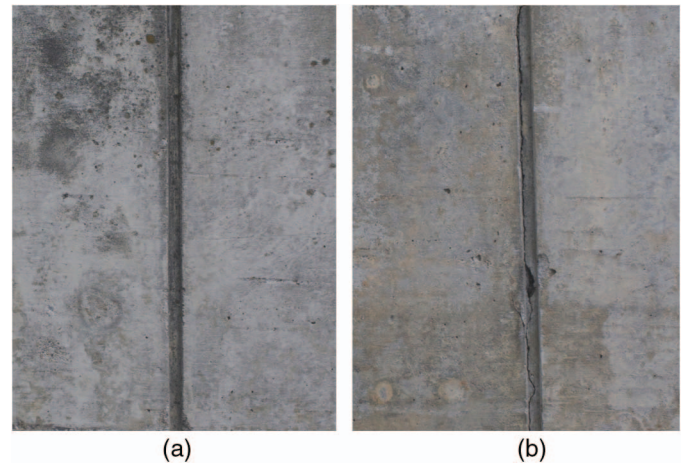


**Fig. 18.** (Color) (a) Intact and (b) cracked areas of a RC retaining wall

The predicted front base width  $w_f$  is formulated by

$$w_f = (r_x)_{F'} \{I|I_{\max}(r^f) \cap L_2\} - (r_x)_{E'} \{I|I_{\max}(r^f) \cap L_1\} \quad (18)$$

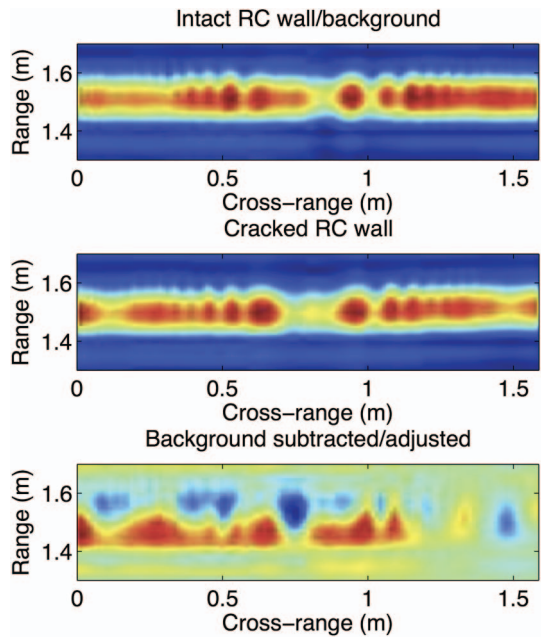
In Table 4, the average predicted front base width is coincidentally the actual width (0.0889 m), with individual errors ranging from 4.63 to 26.75% and absolute average error of 13.3869%.

### Retaining Wall for Crack Imaging

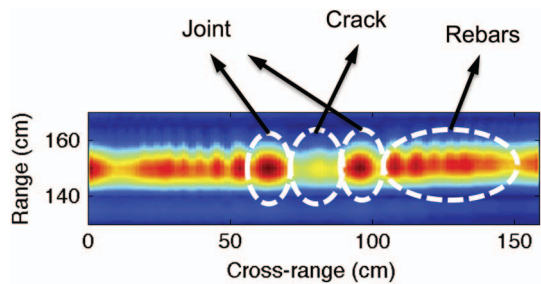
The objective of this test was to use SAR images for characterizing a known crack on a concrete background. A cracked RC retaining wall was selected for crack imaging and an intact region of the RC retaining wall was used for comparison, as shown in Fig. 18. Because the selected crack was at a joint between two RC blocks [Fig. 18(b)], another intact joint was used as the background and for comparison [Fig. 18(a)].

Fig. 19 shows SAR images of intact RC wall (background), cracked RC wall, and their difference (background subtracted). Fig. 20 shows three types of scatterers, representing the scattering effects of (1) two corners of the joint; (2) subsurface rebars; and (3) the crack. These scatterers in the SAR image of the cracked RC retaining wall were identified by comparing with the background SAR image, as shown in Fig. 20. The presence of a concrete crack scatters away the incident radar signal and results in weak reflection in SAR imagery. Two edges of a concrete joint, on the other hand, enhance signal reflection and result in strong response and are imaged by two strong scatterers.

To better analyze the SAR image of a cracked RC retaining wall, background subtraction was applied. However, irregular scatterers were found in Fig. 19 by direct subtraction. This was due to the misalignment of two SAR images. To properly subtract the background image from the target image, the maximum amplitude of specular return of the retaining wall (two scatterers of the joint) was used as a marker in order to adjust the background image



**Fig. 19.** (Color) SAR images of intact and cracked areas on a RC retaining wall



**Fig. 20.** (Color) SAR image of the damaged area on a RC retaining wall

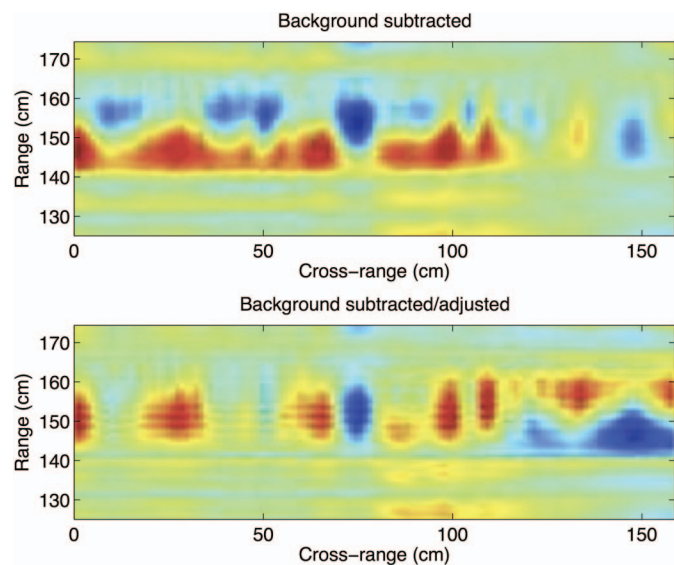


**Fig. 21.** (Color) Adjusted background subtracted SAR image of the cracked area on a RC retaining wall

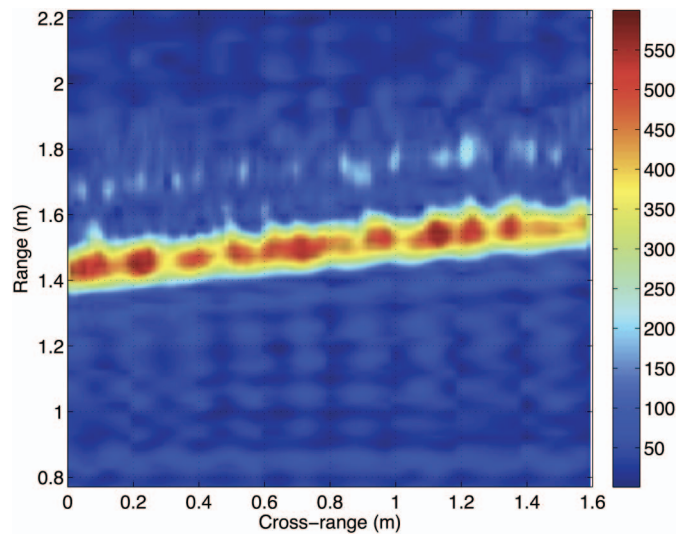


**Fig. 22.** (Color) Identified subsurface interface between bricks and concrete

in background subtraction. In this approach, the specular return of the background image was linearly shifted in the range direction to align it with the specular return of target image. After properly aligning the background image to the target image, better detectability was achieved from background subtraction, as shown in Fig. 21, although some misaligned scatterers still appeared in the cross-range values of 1.2–1.6 m. This example indicates the importance of image alignment for condition assessment using SAR imagery.

## Findings and Discussion

### Subsurface Sensing

In the SAR imaging result of a composite wall at 1.5-m range, subsurface sensing was achieved by identifying an interface between bricks and concrete substrate. Fig. 22 shows the subsurface interface highlighted by a white dashed line. Meanwhile, an approximately 0.1-m (4-in.) subsurface interface between bricks and concrete was identified by the portable imaging radar system at 1.5-m range. This result suggests the detectability of subsurface defects or delamination using the radar system. In other words, detection of subsurface interface and anomalies in the concrete cover region (~0.1 m, with 10 GHz radar signal) can be expected in practice.

### Material Characterization

On the other hand, with a known geometric dimension, materials' electromagnetic properties can be estimated from subsurface sensing. In Fig. 9(a) (range = 5 m), the average distance between the specular return of the wall and the subsurface scatterers was computed to be 0.2357 m. Because the stripmap SAR algorithm used in this paper assumes a free space medium (dielectric constant = 1, nonmagnetic), an equivalent depth  $d_{eqv}$  can be calculated by considering nonfree space medium in the subsurface region of SAR images

$$d_{eqv} = \frac{d_{SAR}}{\sqrt{\epsilon'_r \mu'_r}} \quad (19)$$

where  $d_{SAR}$  = measured depth in SAR images (= 0.2357 m in this case);  $\epsilon'_r$  = dielectric constant (real part of the complex relative

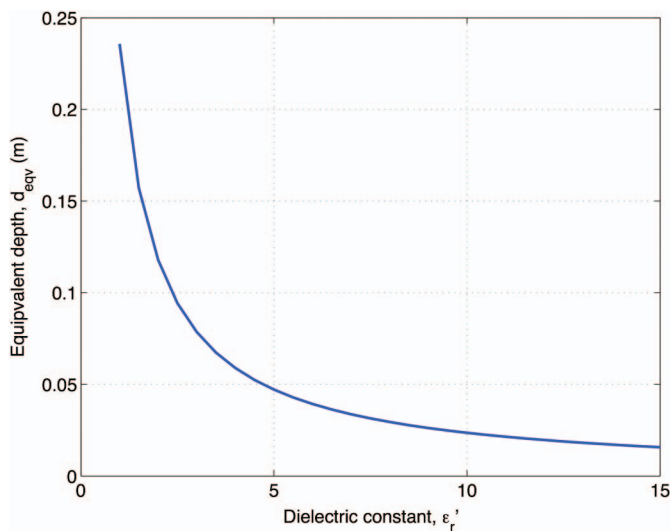


**Fig. 23.** (Color) Relation between  $d_{eqv}$  and  $\epsilon_r'$ —composite wall

electric permittivity) of the subsurface material; and  $\mu_r'$  = real part of the complex relative magnetic permeability. Assuming the bricks to be nonmagnetic, their equivalent electromagnetic properties are  $\mu_r' = 1$  and  $\epsilon_r' = 4$ , resulting in  $d_{eqv} = 0.1178$  m (4.64 in.). Using Eq. (19), the relation between  $d_{eqv}$  and  $\epsilon_r'$  is illustrated by a curve for nonmagnetic media, shown in Fig. 23. In addition, Eq. (15) can be used for predicting the electromagnetic properties of the bricks. Assuming the bricks to be 0.1-m (4-in.) deep and nonmagnetic ( $\mu_r' = 1$ ), the dielectric constant  $\epsilon_r'$  can be calculated to be 5.56.

### Ranging Accuracy Using SAR Images

When using SAR images for ranging a target, specular return from the target was used. As expected, the closer the radar, the stronger was the specular return from the target. A ranging criterion based on maximum SAR amplitude was used to calculate effective range of a target from SAR images. In this on-campus field test, accuracy of the ranging criterion was greater than 98% (error less than 2%) for ranges from 1.5 to 15 m (Fig. 8). Without the interference of a signal scattering effect due to complicated geometry, the ranging accuracy can be very high. In other words, the ranging accuracy is sensitive to the surface geometry and can be used to detect changes in surface geometry in practical applications.

### Effect of Background Noise

The effect of electromagnetic background noise in an outdoor environment was investigated by using the SAR images at different ranges. Ambient electromagnetic background noise depends on the frequency range used, the distance between the radar and noise source(s), and inspection time. Background noise can be stationary or nonstationary in both the time domain and the frequency domain. From the field test result on a brick wall, the authors found that the signal-to-noise ratio (SNR) became less than unity when the range exceeded 4.989 m (Fig. 11), suggesting a threshold range at which background noise suppresses the target signal (specular return of the wall).

### Size Determination

A trapezoidal protrusion on a RC wall was selected for developing size determination criteria. Depth, front base width, and back base width of the trapezoidal protrusion were targeted for determination.

For depth determination [Eq. (15)], the range difference between minimum and maximum SAR amplitudes was used. For back base width estimation, either the intersecting curve criterion [Eq. (16)] or the maximum amplitude criterion [Eq. (17)] provided good width estimates. In the intersecting curve criterion, back base width is computed by the cross-range distance between two intersecting SAR amplitude curves. In the maximum amplitude criterion, back base width was calculated by the cross-range distance between two boundary SAR amplitudes. For front base width determination [Eq. (18)], a step-by-step envelope criterion was developed and front base width was determined by the cross-range distance between two intersecting points. It is important to point out that, due to the scattering effect of radar signals from an irregular geometry (e.g., protrusion), accuracy of size determination can be affected and a wide range of variation can be expected. This suggests the use of additional measurements to reduce the disturbance of the scattering effect in SAR images for size determination. Practically, the size determination of SAR images can be used for structural testing. Currently, most radar systems require the use of perfect electric conductor (PEC) reflectors for size determination and/or ranging, whereas the reported imaging radar system eliminates such a requirement.

### Effect of Concrete Cracking

The presence of a concrete crack was imaged by the radar at 1.5-m range (Fig. 19). The concrete crack scattered the incident radar signal and resulted in weaker reflections. In other words, a weak scatterer on the concrete surface indicates the presence of a crack, when a calibrated background is available. From the reported experimental work, a weaker scatterer could also be attributed to an irregular surface geometry (e.g., concrete spalling). However, the weakening of scatterers in SAR images has different patterns for concrete cracking and concrete spalling. Additional future research is needed to quantify these patterns. The practical use of SAR imaging for detecting concrete cracking lies in the long-term monitoring of concrete structures, for which a reliable background image (without cracking) can be provided.

### Issues with Background Subtraction

The reported field study using an imaging radar demonstrated that background subtraction is instrumental in obtaining clean SAR images for condition assessment. However, there are three issues associated with background subtraction.

1. Representativeness of selected background: To remove the background SAR image from any target image, a representative background must be carefully selected. When conducting field inspection in civil engineering, a perfect background (e.g., identical shape and material property) may not be always available. This suggests the outcome of noisy, background-subtracted SAR images. Denoising techniques will be necessary for improving the resolution of these images.
2. Image misalignment: Even when a perfect background is provided, care must be taken when carrying out background subtraction. Misalignment of SAR images can lead to distorted background-subtracted SAR images. In this result, image adjustment based on the center of specular return appears to be effective in obtaining improved, background-subtracted SAR images.
3. Resolution mismatch: When conducting SAR imaging of structures, image resolution is determined by signal frequency, bandwidth, and cross range. In order to perform meaningful and correct background subtraction, two images must be of the same

resolution to avoid the creation of alias scatterers. This could be an issue in practice because the resolution of SAR images can be different from one location to another for the sake of different inspection purposes. Consistency in image resolution must be ensured before conducting background subtraction.

## Conclusion

This paper reported the performance of surface (ranging, size determination, and crack imaging) and subsurface (interface determination) sensing in field configuration using a portable imaging radar system. All sensing tasks were conducted by using SAR images. Ranging of a composite wall was experimentally achieved from 1.5 to 15 m. Dimensions of a trapezoidal concrete protrusion were identified from SAR images. The presence of a concrete crack was imaged by a weak scatterer in SAR images. A subsurface composite interface was detected in SAR images. Subsurface sensing was used to estimate the electromagnetic property of materials. In these tests, effect of background noise became dominant when the range exceeded 4.989 m, suggesting the need to remove background noise. Issues such as representativeness of background and image misalignment are important when performing background subtraction. The paper proposed image-based, quantitative condition assessment criteria for ranging and size determination.

## Acknowledgments

The research reported in this paper is supported by the U.S. Department of Transportation, Office of the Assistant Secretary for Research and Technology (OST), through Commercial Remote Sensing and Spatial Information (CRS&SI) under Grant OASRTS-14-H-UML (Program Manager, Caesar Singh). The authors also thank undergraduate students Reny Reny Yohana Lende Mere and Thet Myat Noe Sein for their assistance in conducting field tests.

## Disclaimer

The views, opinions, findings, and conclusions reflected in this paper are the responsibility of the authors only and do not represent the official policy or position of the USDOT/OST-R, or any State or other entity.

## References

Bennett, P. J., and Rutz, F. R. (2012). "Structural health monitoring with interferometric radar." *Forensic Engineering 2012: Gateway to a Safer Tomorrow*, ASCE, Reston, VA, 28–37.

Bungey, J. H. (2004). "Sub-surface radar testing of concrete: A review." *Constr. Build. Mater.*, 18(1), 1–8.

Carrara, W. G., Goodman, R. S., and Majewski, R. M. (1995). *Spotlight synthetic aperture radar—Signal processing algorithms*, Artech House, Boston.

Cheney, M. (2001). "A mathematical tutorial on synthetic aperture radar." *SIAM Rev.*, 43(2), 301–312.

Cumming, I. G., and Wong, F. H. (2005). *Digital processing of synthetic aperture radar data—Algorithms and implementation*, Artech House, Boston.

Daniels, D. J. (2007). *Ground penetrating radar*, 2nd Ed., Institution of Engineering and Technology, London.

Desai, M. D., and Jenkins, W. K. (1992). "Convolution backprojection image reconstruction for spotlight mode synthetic aperture radar." *IEEE Trans. Image Process.*, 1(4), 505–517.

Ganguli, A., Rappaport, C. M., Abramo, D., and Wadia-Fascetti, S. (2012). "Synthetic aperture imaging for flaw detection in a concrete medium." *NDT&E Int.*, 45(1), 79–90.

Hoegh, K., and Khazanovich, L. (2015). "Extended synthetic aperture focusing technique for ultrasonic imaging." *NDT&E Int.*, 74, 33–42.

Jol, H. M. (2009). *Ground penetrating radar: Theory and applications*, Elsevier, Amsterdam, Netherlands.

Kak, A. C., and Slaney, M. (2001). *Principles of computerized tomographic imaging*, SIAM, Philadelphia.

Kong, J. A. (2000). *Electromagnetic wave theory*, EMW Publishing, Cambridge, MA.

Krause, M., Mielentz, F., Milman, B., Muller, W., Schmitz, V., and Wiggenhauser, H. (2001). "Ultrasonic imaging of concrete members using an array system." *NDT&E Int.*, 34(6), 403–408.

LabVIEW [Computer software]. National Instruments, Austin, TX.

Pieraccini, M., et al. (2004). "Remote sensing of building structural displacements using a microwave interferometer with imaging capability." *NDT&E Int.*, 37(7), 545–550.

Rehman, S. K. U., Ibrahim, Z., Memon, S. A., and Jameel, M. (2016). "Nondestructive test methods for concrete bridges: A review." *Constr. Build. Mater.*, 107(3), 58–86.

Rhim, H., and Buyukozturk, O. (2000). "Wideband microwave imaging of concrete for nondestructive testing." *J. Struct. Eng.*, 10.1061/(ASCE)0733-9445(2000)126:12(1451), 1451–1457.

Sansalone, M., and Street, W. B. (1997). *Impact-echo nondestructive evaluation of concrete and masonry*, Bullbrier Press, Ithaca, NY.

Schickert, M., Krause, M., and Muller, W. (2003). "Ultrasonic imaging of concrete elements using reconstruction by synthetic aperture focusing technique." *J. Mater. Civil Eng.*, 10.1061/(ASCE)0899-1561(2003)15:3(235), 235–246.

Shinozuka, M., Ghanem, R., Houshmand, B., and Mansouri, B. (2000). "Damage detection in urban areas by SAR imagery." *J. Eng. Mech.*, 10.1061/(ASCE)0733-9399(2000)126:7(769), 769–777.

Soumekh, M. (1999). *Synthetic aperture radar signal processing with MATLAB algorithms*, Wiley, New York.

Yu, T. (2011). "Distant damage-assessment method for multilayer composite systems using electromagnetic waves." *J. Eng. Mech.*, 10.1061/(ASCE)EM.1943-7889.0000257, 547–560.

Yu, T. (2016). "Quantitative assessment of CFRP-concrete cylinders using synthetic aperture radar images." *Res. Nondestruct. Eval.*, 1–18.

Yu, T., and Buyukozturk, O. (2008). "A far-field airborne radar NDT technique for detecting debonding in GFRP-retrofitted concrete structures." *NDT&E Int.*, 41(1), 10–24.

Yu, T., Cheng, T. K., Zhou, A., and Lau, D. (2016). "Remote defect detection of FRP-bonded concrete system using acoustic-laser and imaging radar techniques." *Constr. Build. Mater.*, 109, 146–155.